



**HAL**  
open science

# Dynamics of detonation transmission and propagation in a curved chamber: a numerical and experimental analysis

J. Melguizo-Gavilanes, V. Rodriguez, P. Vidal, R. Zitoun

## ► To cite this version:

J. Melguizo-Gavilanes, V. Rodriguez, P. Vidal, R. Zitoun. Dynamics of detonation transmission and propagation in a curved chamber: a numerical and experimental analysis. *Combustion and Flame*, 2021, 223, pp.460-473. 10.1016/j.combustflame.2020.09.032 . hal-02989959

**HAL Id: hal-02989959**

**<https://hal.science/hal-02989959>**

Submitted on 5 Nov 2020

**HAL** is a multi-disciplinary open access archive for the deposit and dissemination of scientific research documents, whether they are published or not. The documents may come from teaching and research institutions in France or abroad, or from public or private research centers.

L'archive ouverte pluridisciplinaire **HAL**, est destinée au dépôt et à la diffusion de documents scientifiques de niveau recherche, publiés ou non, émanant des établissements d'enseignement et de recherche français ou étrangers, des laboratoires publics ou privés.

# Dynamics of detonation transmission and propagation in a curved chamber: a numerical and experimental analysis

J. Melguizo-Gavilanes, V. Rodriguez, P. Vidal, R. Zitoun

*Institut Pprime, UPR 3346 CNRS, Fluids, Thermal Science and Combustion  
Department, 86961 Futuroscope-Chasseneuil, France*

---

## Abstract

The dynamics of detonation transmission from a straight channel into a curved chamber was investigated numerically and experimentally as a function of initial pressure ( $10 \text{ kPa} \leq p_0 \leq 26 \text{ kPa}$ ) in an argon diluted stoichiometric  $\text{H}_2\text{-O}_2$  mixture. Numerical simulations considered the two-dimensional reactive Euler equations with detailed chemistry; hi-speed schlieren and  $\text{OH}^*$  chemiluminescence were used for flow visualization. Results show a rotating Mach detonation along the outer wall of the chamber and the highly transient sequence of events (i.e. detonation diffraction, re-initiation attempts and wave reflections) that precedes its formation. An increase in pressure, from 15 kPa to 26 kPa, expectedly resulted in detonations that are less sensitive to diffraction. The decoupling location of the reaction zone and the leading shock along the inner wall determined where transition from regular reflection to a rather complex wave structure occurred along the outer wall. This complex wave structure includes a rotating Mach detonation (stem), an

---

\*Corresponding author: [josue.melguizo-gavilanes@cnrs.pprime.fr](mailto:josue.melguizo-gavilanes@cnrs.pprime.fr)

incident decoupled shock-reaction zone region, and a transverse detonation that propagates in pre-shocked mixture. For lower pressures, i.e.  $\leq 10$  kPa, the detonation fails shortly after ignition. However, the interaction of the decoupled leading shock with the curved section of the chamber results in detonation initiation behind the *inert* Mach stem. Thereafter, the evolution was similar to the 15 kPa case. Simulations and experiments qualitatively and quantitatively agree indicating that the global dynamics in this configuration is mostly driven by the geometry and initial pressure, and not by the cellular structure in highly compressed regions.

*Keywords:* Detonation dynamics, Mach reflection, re-initiation, detailed chemistry, high speed visualization, numerical simulation, OpenFOAM

---

## 1. Introduction

Understanding detonation interactions with curved geometries is necessary to propulsion and industrial and nuclear safety. Regarding propulsion, effort has been invested in developing prototypes of pulse and continuously rotating detonation engines (RDE), though many questions remain unanswered about design, integrity, control, vibration, noise, etc. [1, 2, 3]. Regarding safety, most of the work has been devoted to prevention and mitigation of ignition, flame acceleration and detonation hazards. In mining industries, chemical processing and nuclear power plants, fuel leaks and accidental ignitions in congested or confined spaces can have devastating consequences such as losses of lives, infrastructure destruction, and high environmental impact [4].

The simplest RDE chamber is the annular space between two coaxial

cylinders in which one or several detonation waves propagate azimuthally consuming the reactive mixture. Promising RDE geometries are the hollow and semi-hollow configurations in which the internal wall of the combustor is fully or partially removed, resulting in larger specific impulse, pressure and rotation frequencies, e.g., [5]. Literature includes experimental, numerical and theoretical studies on detonation propagation inside annular RDEs [6, 7, 8], curved channels/chambers of constant and varying widths [9, 10, 11, 12, 13, 14, 15, 16], wedges and bends [17], and U-bend tubes [18]. Loss-of-coolant accidents in nuclear reactors may result in significant releases of hydrogen and the generation of flammable atmospheres that accumulate between the containment and the curved reactor building [19].

In the present study, a simplified hollow geometry amenable to fundamental analysis is used, namely a straight channel connected to a curved chamber with a small center body. The wave dynamics in this configuration is presumably representative of the early stages of detonation propagation inside a hollow RDE, and of that close to a curved wall of an industrial reactor.

Recently, this geometry was experimentally studied using a stoichiometric propane-oxygen mixture [9, 10]. Its primary finding is a steadily rotating overdriven detonation wave along the outer wall of the chamber, whose distinguishing features are: (i) a Mach wave; (ii) a quasi-steady rotation velocity; (iii) an almost constant Mach stem height, and (iv) very small detonation cells oriented parallel to the wall in the highly compressed regions behind the Mach front. Low-order modeling using Geometrical Shock Dynamics (GSD) [20] was capable of reproducing qualitatively the main global features

in the chamber, i.e, wave diffraction and reflections, and a steadily rotating Mach wave. However, quantitatively capturing the details of the complex experimental transients requires unsteady, time accurate simulations.

The main objective of the present work is thus to numerically characterize the flow dynamics inside a curved chamber as a function of initial pressure and to interpret the results based on comparisons with our experimental data. An argon-diluted stoichiometric  $\text{H}_2\text{-O}_2$  mixture is considered for which the implementation of a reliable detailed chemical kinetics scheme makes computations both tractable and representative, thereby reducing uncertainties on what modeling should be used for this rich phenomenological configuration.

## 2. Experimental Methodology

### 2.1. Apparatus and procedure

The experimental apparatus is shown in Fig. 1, it includes a detonation tube, a curved chamber and an expansion vessel. After vacuuming, the entire system is filled with a premixed  $2\text{H}_2\text{:O}_2\text{:2Ar}$  mixture at the desired initial pressure  $p_0$ .

A deflagration is ignited at one end of the tube and accelerates to detonation by means of a Shchelkin spiral before entering the curved chamber. In all experiments, the steady Chapman-Jouguet (CJ) regime was reached. This was verified by several dynamic pressure transducers (P1-P4) that recorded the pressure evolution behind the wave front to obtain an average detonation velocity ( $D_{\text{CJ}}$ ). The detonation tube is 2-m long and has a 51-mm inner diameter. The detonation enters the curved chamber through a 200-mm long straight section with a 30-mm  $\times$  20-mm cross-section. The detonation then

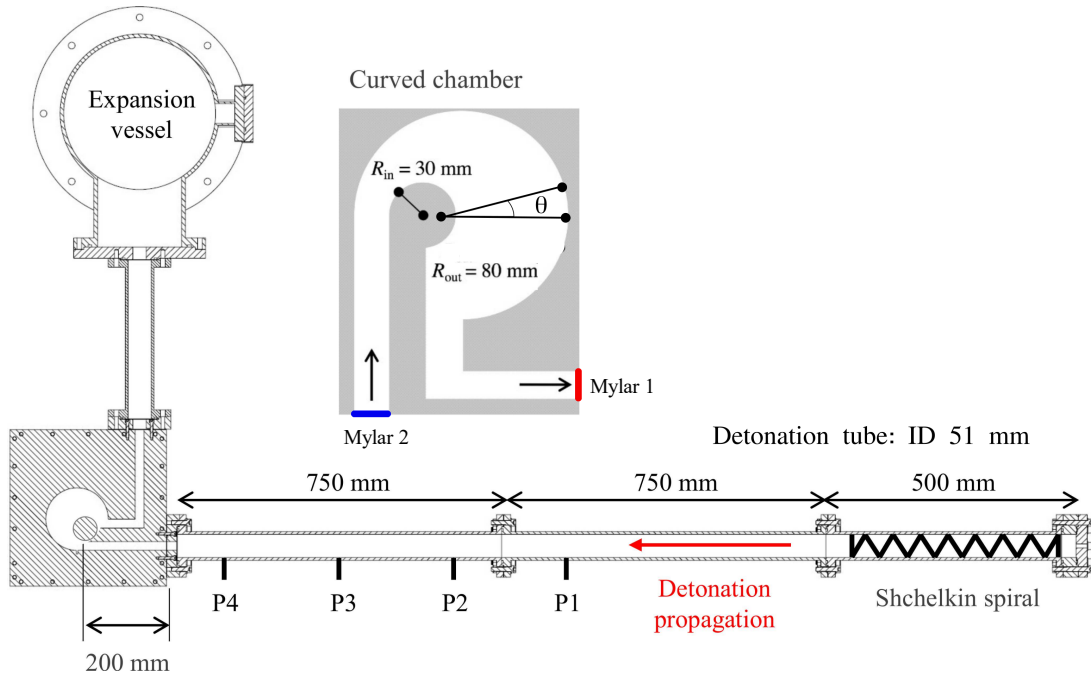


Figure 1: Schematic of experimental setup showing the detonation tube, the curved chamber and the expansion vessel. The angular position,  $\theta$ , is measured counterclockwise from the positive  $x$ -axis. Note that Mylar 1 is used for all experiments whereas Mylar 2 is put in place for inert shots only. Adapted from Ref. [9].

diffraction in a larger volume bounded by a 80-mm radius outer wall and a small 30-mm radius inner wall. The combustion products finally expand inside a large vessel which is separated from the curved chamber by a 18- $\mu\text{m}$  Mylar foil (Mylar 1). More details on the experimental apparatus and procedure are given in [9, 10].

## 2.2. Flow visualization

The curved chamber allows for 217-mm  $\times$  275-mm optical access with one UV-silica window on one face and a borosilicate-crown glass window on

the other face, both 27-mm thick. Two visualization techniques were used to investigate the dynamics: (i) chemiluminescence based on the hydroxyl radical ( $\text{OH}^*$ ) to resolve the overall evolution, and (ii) schlieren to focus on details of interest. Both were coupled to hi-speed cameras.

$\text{OH}^*$  visualizations were performed using an intensified Princeton PI-MAX4 camera operated in dual frame imaging mode with a OH filter centered on  $311 \pm 5$  nm. Two pictures were recorded per shot separated by a 10- $\mu\text{s}$  delay. The full-frame resolution was  $1024 \times 1024$  pixels with a 100-ns exposure time. The experimental sequences shown in Figs. 2 and 3 are thus a composite of three shots per initial pressure. This visualization technique has been extensively used as a typical combustion marker [21, 22, 23, 24]. Its main limitation is that excited OH molecules have relatively long life times (compared to detonation time scales) and remain active in burnt gases. This can make the interpretation of the images difficult, especially, in the center of the chamber where different combustion processes interact, i.e., decoupled leading shock-reaction zone, and detonations.

Schlieren visualizations were performed using a mercury-vapor lamp and a Shimadzu HPV-X2 camera. Videos were recorded at 500 kHz with an exposure time of 200 ns.

### **3. Computational methodology**

#### *3.1. Governing equations and numerical methods*

The flow field in the curved chamber was modeled using the reactive Euler equations with detailed chemistry and temperature dependent thermodynamics (i.e. JANAF tables to compute species/mixture heat capacities,

enthalpies and entropies) [25]. The governing equations were solved in a two-dimensional planar geometry using the OpenFOAM Toolbox [26]; chemical kinetics was modeled with the 9-species, 21-reactions Mével’s mechanism for hydrogen-oxidation [27], whose ignition delay time predictions (metric of interest in the current study) are neither the fastest nor the slowest among the available alternatives. The spatial discretization of the solution domain is performed using finite volumes (FV) which allows for body-fitted hexagonal meshes that avoid the staircasing present when numerically integrating curved geometries with finite differences. The solver includes a hybrid implementation for the numerical fluxes that make it suitable for a wide range of Mach numbers; this is achieved by combining PISO methods (i.e. pressure-velocity coupling) in regions with low flow velocities ( $M \leq 0.3$ ), together with standard techniques for high speed flows (i.e. flux-splitting and limiters). Here, due to the nature of the flow at hand, only the latter scheme is active. The numerical fluxes at cell-faces are thus computed using a central-upwind Kurganov-Tadmor scheme [28, 29]. The flow variables on cell faces are reconstructed through a second-order interpolation with a symmetric van Albada flux limiter which results in non-oscillatory bounded transitions across shocks and contact discontinuities. The chemical source terms are computed using a stiff ODE solver (i.e. fourth-order Rosenbrock). The PBiCGStab (Preconditioned Biconjugate Gradient Stabilized) method is used for all the linear systems resulting from the discretization of the governing equations, preconditioned through the DILU (Diagonal Incomplete-LU) technique. Finally, the time integration uses a second order Crank-Nicolson method, and the time step is dynamically adapted during

the computation with an acoustic Courant number of 0.5 to ensure stability of the numerical scheme. The implementation, verification and validation of this solver follows the methodology presented in [30]; the verification stage used standard methodologies in which the hydrodynamic and chemical parts of the solver are independently tested. For the combined implementation, unsteady 1-D simulations of detonations were carried out to reproduce their well-documented non-linear dynamics [31].

### 3.2. Domain, initial and boundary conditions

The computational domain is shown in Figs. 2 and 3, and reproduces the curved chamber shown in Fig. 1. Four initial pressures were considered  $p_0 = 10, 15, 20$  and  $26$  kPa to investigate the detonation dynamics in the chamber as a function of increasing pressure. Initial conditions were quiescent mixture at  $T_0 = 288$  K, and mass fractions  $Y_{\text{H}_2} = 0.034779$ ,  $Y_{\text{O}_2} = 0.276021$ ,  $Y_{\text{Ar}} = 0.6892$ , corresponding to a stoichiometric  $\text{H}_2\text{-O}_2$  mixture with  $\% \text{Ar}_{\text{vol}} = 40$ . A slip boundary condition for velocity, and zero gradient for temperature, species and pressure were imposed on the chamber walls. A hexagonal uniform mesh was used comprising 9,286,953 cells, which resulted in resolutions of 15, 10, 8, 5 points per ZND induction length,  $l_{\text{ind}}$ , for  $p_0 = 10, 15, 20, 26$  kPa, respectively. Simulations were run using 200 processors, and took approximately 10,000 CPU hours per case. The detonations were ignited by imposing three equally spaced hemi-spherical regions ( $r = 2.5$  mm) of high pressure ( $p_{\text{ign}}/p_0 \sim 46$ ) and temperature ( $T_{\text{ign}}/T_0 \sim 14$ ) at the chamber inlet whose width is 30 mm. This initiation method resulted in steadily propagating cellular detonation fronts before the curved section of the chamber (see numerical soot foils in Fig. 4, and first speed data points

along the outer wall in Figs. 5 and 6), except for  $p_0 = 10$  kPa.

## 4. Results and discussion

The numerically predicted and experimentally observed dynamics of the detonation as it propagated through the curved chamber is presented below as a function of initial pressure,  $p_0$ . Only results for  $p_0 = 15$  kPa and 26 kPa are discussed in subsections 4.1-4.3 because the intermediate pressure case was not found to provide additional insight. Subsection 4.4 describes the re-initiation dynamics for  $p_0 = 10$  kPa.

### 4.1. Overall dynamics

Figure 2 shows a time sequence of pressure contours superimposed on H atom numerical fields together with experimental OH\* chemiluminescence for  $p_0 = 15$  kPa. H atom is a useful chemical activity marker because of its short life time; it peaks inside the reaction zone and quickly decays thereafter, as seen from one-dimensional ZND profiles. The times reported elapse from the initiation of the detonation at the chamber inlet in the numerical simulations.

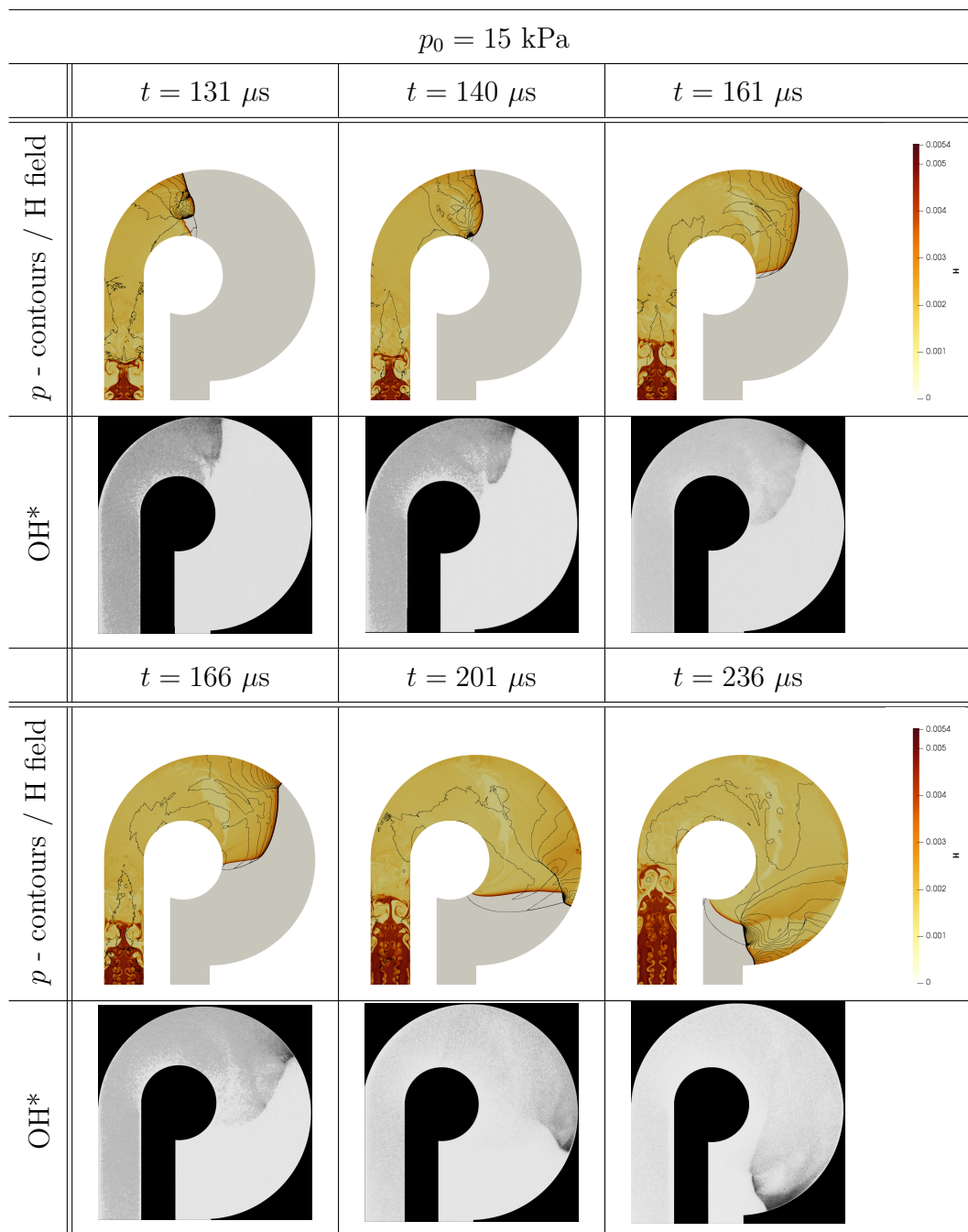


Figure 2: Overall dynamics for  $p_0 = 15 \text{ kPa}$ : numerical pressure contours and H atom field vs. experimental OH\* chemiluminescence.

For  $131 \mu\text{s} \leq t \leq 166 \mu\text{s}$ , the numerical results show a diffracting detonation front, a subsequent transverse detonation wave that consumes shocked reactive mixture, early stages of decoupling of the leading shock (LS) and reaction zone (RZ) along the inner wall, and the formation of a reactive Mach stem along the outer wall. The experimental images show the regions where chemical reactions are strong. Initially ( $131 \mu\text{s} \leq t \leq 140 \mu\text{s}$ ),  $\text{OH}^*$  is widely spread in the chamber; at later times ( $140 \mu\text{s} \leq t \leq 166 \mu\text{s}$ ), the highest  $\text{OH}^*$  intensity is confined to the outer wall characterized by a black thick line normal to the outer wall representing a Mach detonation front. Inside the chamber, the signal decreases as the combustion front continues to propagate. The last two times of the sequence display the most interesting dynamics with strong chemical activity obliquely attached to the triple point of the Mach stem at  $t = 201 \mu\text{s}$ , and an “S-shape” structure at  $t = 236 \mu\text{s}$ . The numerical fields provide insight into the emergence of these structures. They arise from the interaction of the Mach detonation front with the shocked reactive gas left behind upon the final decoupling of the initial detonation front along the inner wall. A new combustion front propagates in this region consuming the mixture. The bright red regions in the straight section of the numerical domain are remnants of the initiation.

Figure 3 shows the same numerical and experimental fields for  $p_0 = 26$  kPa. The dynamics of the detonation front is strongly affected by the pressure increase. Notably, the detonation front is less sensitive to the initial area change as it encounters the curved region of the chamber. For  $t \geq 143 \mu\text{s}$  full decoupling of the LS and RZ occurs along the inner wall, whereas a regular reflection establishes itself along the outer wall until the last time shown in

Fig. 3. Experimental OH\* fields show a curved transmitted detonation with high intensity regions corresponding to triple-point collisions along the front (see  $t = 133\text{--}143\ \mu\text{s}$ ). At later times ( $t \geq 161\ \mu\text{s}$ ), the only region with strong OH\* production is located where the regular reflection takes place, and is bounded behind by a tailing reflected wave and the outer wall. Additional details about later stages of propagation are provided in subsection 4.3.

Numerical soot foils obtained by tracking the pressure maxima in the computational domain at each time step are presented in Fig. 4. They provide a history of the triple point trajectories during detonation transmission, and offer insight into local quenching, and re-initiation events. Bright white lines of varying thicknesses represent high pressure regions. The sensitivity to diffraction with increasing pressure is clearly depicted in the figure. For  $p_0 = 15\ \text{kPa}$ , decoupling occurs immediately upon reaching the curved section of the chamber. For  $p_0 = 26\ \text{kPa}$ , the cells of increasing length along the inner wall of the chamber are a signature of consecutive decoupling and re-coupling events characterized by combustion fronts that propagate inside these shocked reactive regions. Additionally, numerical soot foils allow to uniquely determine the location where regular-to-Mach detonation transitions take place. Experiments confirm this observation by the presence of fine detonation cells in these regions [9, 10]. It should be noted that while the numerically predicted decrease in cell size,  $\lambda$ , as a function of increasing initial pressure  $p_0$  is the same as that reported experimentally for the mixture studied [32], the actual value of  $\lambda$  is underpredicted in the present computations ( $\lambda_{\text{exp}}/\lambda_{\text{sim}} \sim 3.5$ ). Vibrational non-equilibrium effects [33, 34] and/or reaction model uncertainties are potential explanations; three-dimensional

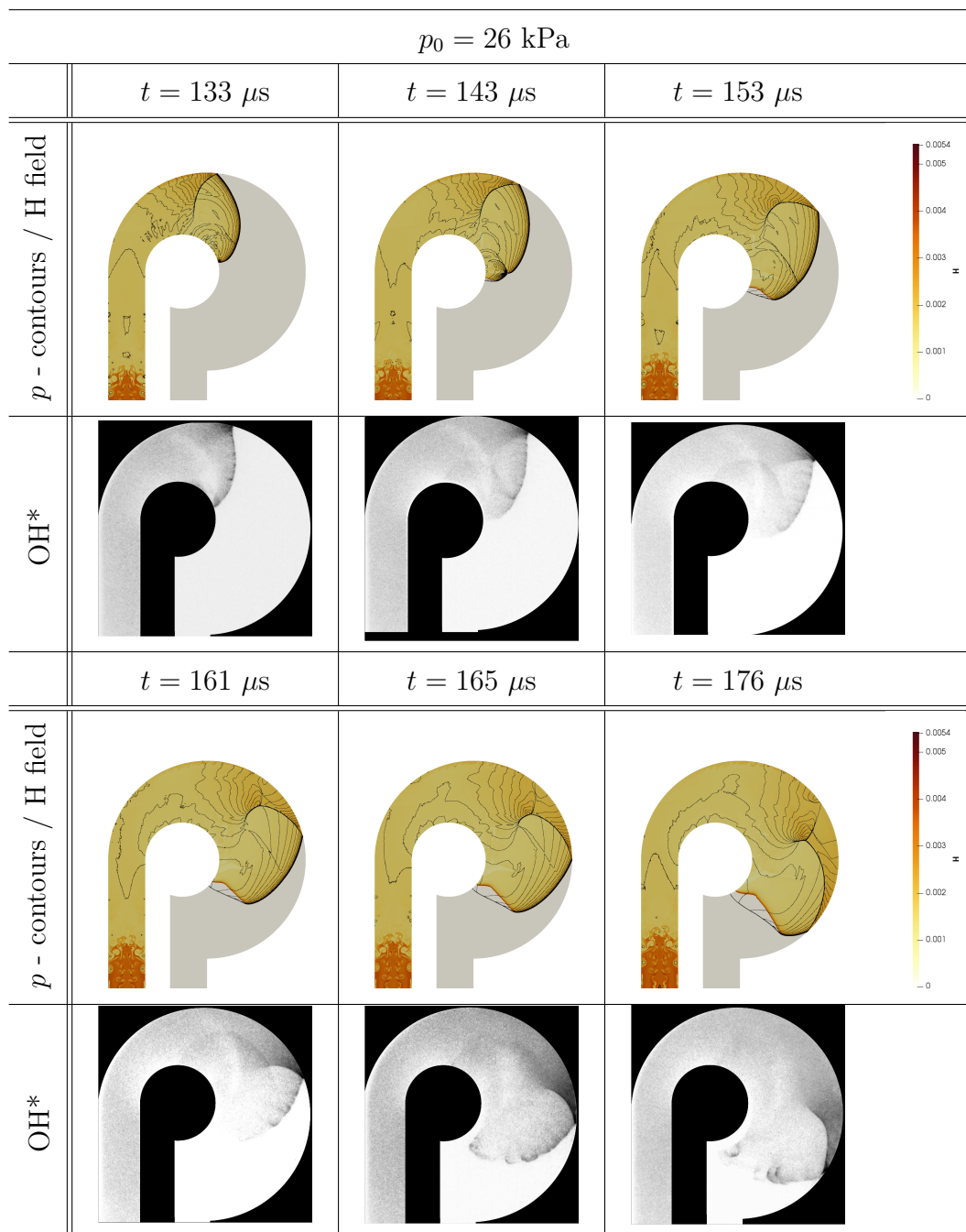


Figure 3: Overall dynamics for  $p_0 = 26 \text{ kPa}$ : numerical pressure contours and H atom field vs. experimental OH\* chemiluminescence.

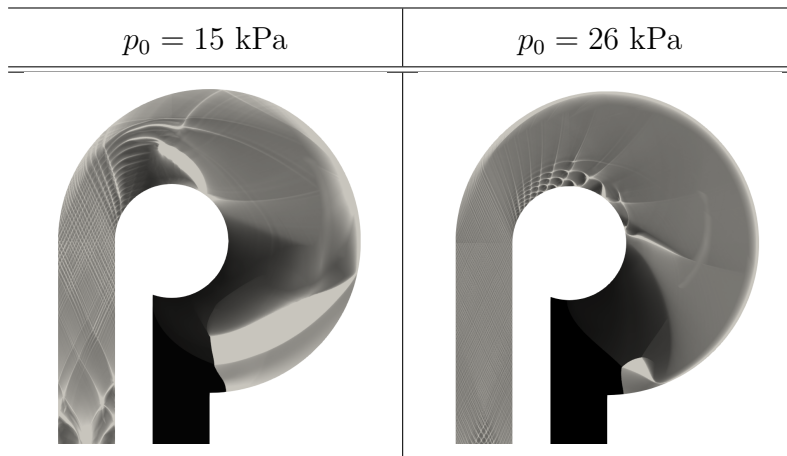


Figure 4: Numerical soot-foils.

effects have been found to result in a  $\lambda$  decrease when compared to two-dimensional simulations [35].

Figures 5 and 6 show the position and speed of the LS and RZ are reported as a function of time along the outer and inner walls. The angular normalized position,  $\theta/\pi$ , is measured counterclockwise from the positive  $x$ -axis (i.e.  $\theta/\pi = 0$ ); see Fig. 1. Following this convention, the detonation propagates from the II ( $\theta/\pi = 1.0$ ) to the IV ( $\theta/\pi = -0.5$ ) quadrant during its transit through the chamber. Samples were collected at a frequency of 1 MHz ( $1 \mu\text{s}$ ).

The evolution along the outer wall is qualitatively similar for 15 kPa and 26 kPa, showing unnoticeable decoupling between the LS and RZ, followed by significant acceleration/deceleration of the front. The velocity peaks shown in Figs. 5 and 6 are attained during propagation as a regular reflection, whereas the transition from regular-to-Mach detonation is accompanied by a decrease in the front propagation speed. For  $p_0 = 15 \text{ kPa}$ , the final wave structure (“S-shape”) is overdriven and accelerates linearly for  $t \geq 200 \mu\text{s}$  reaching an

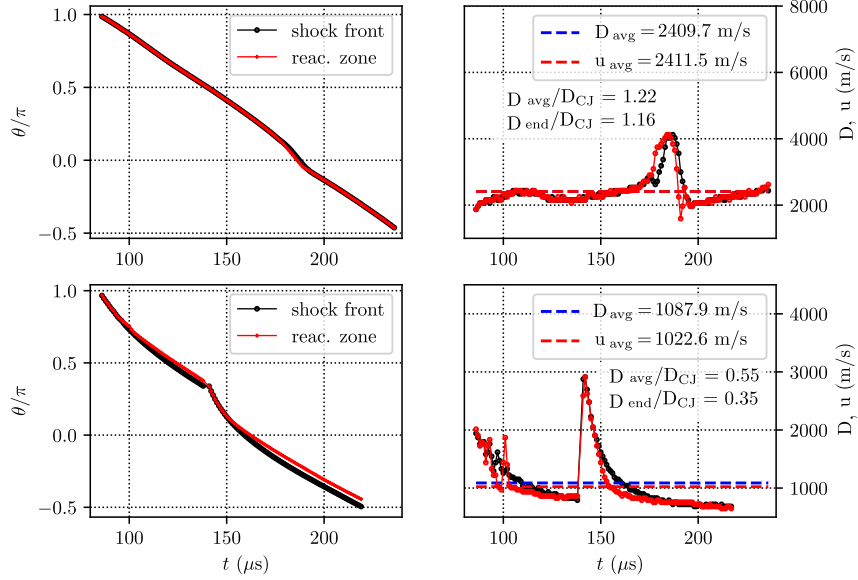


Figure 5: Wave positions and speeds histories along outer (top) and inner (bottom) walls for  $p_o = 15$  kPa. The steady detonation propagation velocity,  $D_{CJ} = 1971$  m/s;  $D_{\text{avg}}$  and  $u_{\text{avg}}$  are the leading shock and reaction zone average propagation velocity over the entire sampling period.  $D_{\text{end}}/D_{CJ}$  is the average normalized propagation velocity measured after the final wave complex is established, i.e.,  $t \geq 200 \mu\text{s}$ .

average normalized propagation speed of  $D_{\text{end}}/D_{CJ} \sim 1.16$ ; this observation is in line with our previous findings using a stoichiometric propane-oxygen mixture [9]. For  $p_0 = 26$  kPa, the velocity signal ends shortly after the deceleration period due to the arrival of the wave to the end of the curved section.

The evolution along the inner wall exhibits more interesting dynamics. For  $p_0 = 15$  kPa smooth decoupling of the LS and RZ as the detonation enters the curved chamber, subsequent re-coupling as the transverse detonation, shown in Fig. 2 at  $t = 131 \mu\text{s}$ , reaches the inner wall, followed, once again,

by smooth decoupling as the detonation propagates into a diverging area. The velocity profiles, for  $p_0 = 15$  kPa and 26 kPa, show the signature of a single re-coupling event for the former, and the consecutive decoupling/re-coupling events referred to earlier for the latter. A resolution study on the wave position, speed histories and particularly, on the location where the transition from regular-to-Mach detonation takes place along the outer wall, revealed that at least 10 pts per  $l_{\text{ind}}$  are required to capture the experimentally observed structure at the end of the chamber for  $p_0 = 15$  kPa. For higher pressures,  $p_0 = 26$  kPa, in which the diffraction and re-initiation transients are less pronounced, a resolution of 5 pts per  $l_{\text{ind}}$  was found to be sufficient.

#### *4.2. Early stages of propagation*

Figure 7 shows a close-up of the early stages of detonation diffraction for  $p_0 = 15$  kPa. A planar detonation front first enters the curved chamber and, close to the inner wall, its RZ begins to decouple from the LS due to the propagation of expansion waves originating from the region where the front first encounters an area increase (see  $96 \mu\text{s} \leq t \leq 101 \mu\text{s}$ ). The high sensitivity of chemical reaction rates to decreasing temperature results in significantly longer induction times behind the leading shock at lower temperature. These waves propagate perpendicular to the detonation front towards the outer wall making it curved. An increased detonation front curvature results in a faster local temperature and velocity decrease, so the reaction zone further decouples from the leading shock ( $111 \mu\text{s} \leq t \leq 131 \mu\text{s}$ ).

Along the outer wall, the detonation appears to be undisturbed initially but quickly transits to a Mach reflection with the leading shock normal to the wall (see  $t = 111 \mu\text{s}$ ). Detonation and shock wave reflection types (i.e.

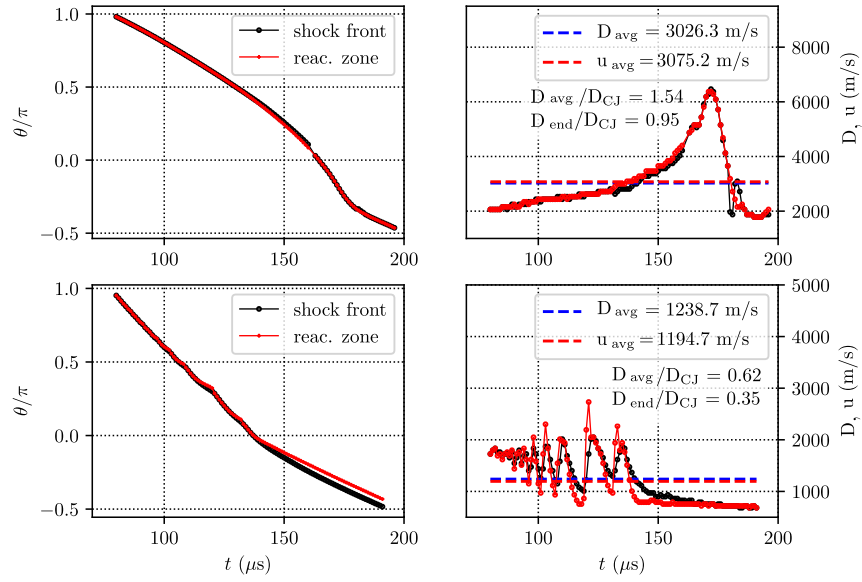


Figure 6: Wave positions and speeds histories along outer (top) and inner (bottom) walls for  $p_o = 26$  kPa. The steady detonation propagation velocity,  $D_{CJ} = 1993$  m/s;  $D_{\text{avg}}$  and  $u_{\text{avg}}$  are the leading shock and reaction zone average propagation velocity over the entire sampling period.  $D_{\text{end}}/D_{CJ}$  is the average normalized propagation velocity measured after the final wave complex is established, i.e.,  $t \geq 180 \mu\text{s}$ .

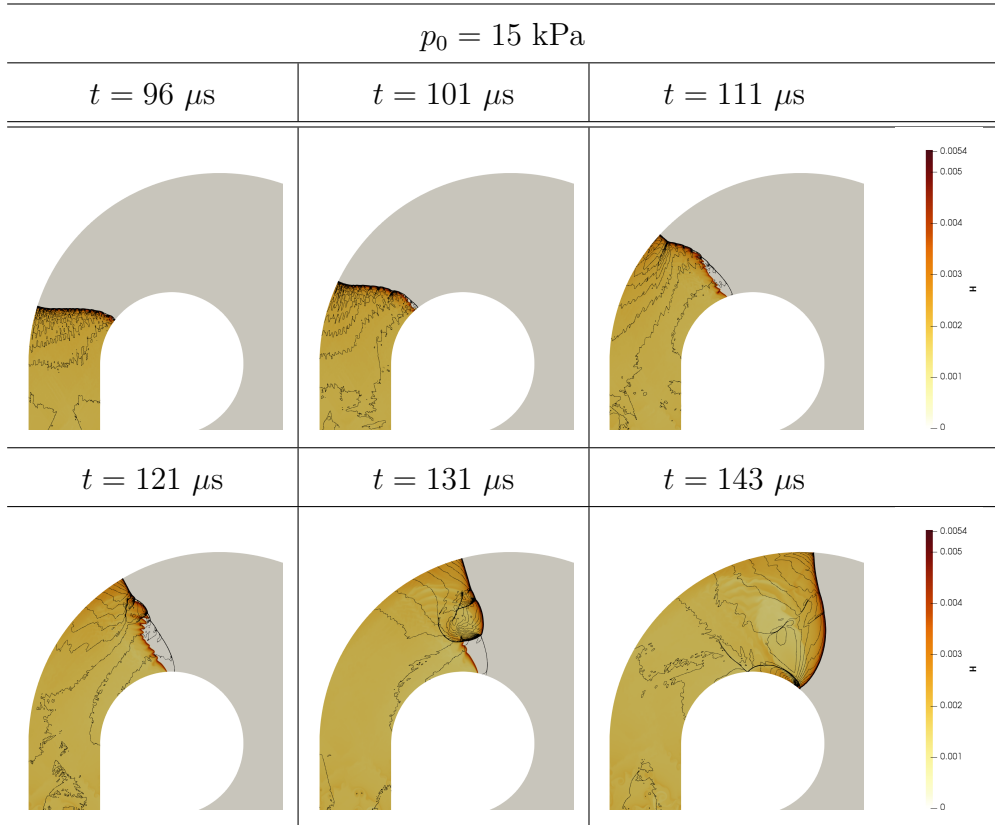


Figure 7: Early stages of detonation propagation for  $p_0 = 15 \text{ kPa}$ : numerical pressure contours and H atom field.

regular or Mach) upon interactions with concave wedges/cylinders have been studied extensively. They are known to depend on the wedge angle/cylinder radius, front velocity and mixture characteristics [17, 36, 37]. After the initial Mach stem is established, it grows, reaches a maximum and decreases. The increased pressure and temperature behind the stem results in induction lengths that can be orders of magnitude smaller than the reference steady ZND length, so the cell size significantly decreases. In these highly com-

pressed regions the numerical resolution used in this work does not resolve the detonation structure, but is able to capture all the transient dynamics in the chamber. While the importance of the cellular structure of detonation fronts close to propagation limits is now widely accepted, the cellular pattern left behind this specific overdriven Mach detonation front is so small that a fair approximation is to neglect it, which provides supporting evidence to the applicability of GSD modeling for the analysis of the current configuration [20], and also suggests that the chemical kinetics may not be the main aspect driving this element of the phenomenon. These important features are further discussed in the last section.

Figure 7 ( $111 \mu\text{s} \leq t \leq 131 \mu\text{s}$ ) also indicates that the first re-initiation mechanism appears to be driven by the competition among reflected expansions from the outer wall, compression waves from downward traveling triple points, and the progress of the decoupled LS-RZ. A re-initiation center, and the birth of a combustion front that subsequently consumes shocked mixture are visible at  $t = 121 \mu\text{s}$ . The structure of this combustion front ( $t = 131 \mu\text{s}$ ) is analogous to detonations propagating under yielding confinement, namely a curved front, a transmitted shock and a shear layer [38, 39]. A closeup of this structure is shown in Fig. 8. Upon reflection from the inner wall,  $t = 143 \mu\text{s}$ , the early stages of a Mach detonation is shown whose typical features are a Mach stem, an incident curved detonation, and a shear layer.

Figure 9 clearly displays the effect of increasing initial pressure on the early dynamics. As mentioned above, the sensitivity to area changes is significantly decreased for  $p_0 = 26 \text{ kPa}$ . The detonation front becomes curved in the inner region due to the numerous expansions emanating from the inner

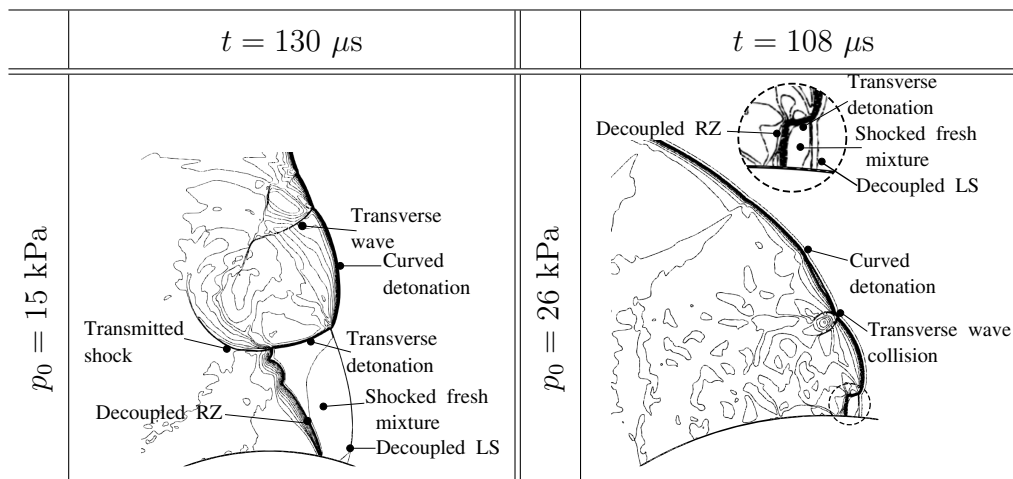


Figure 8: Close up to detonation diffraction structure close to inner wall for increasing pressure; solid lines are temperature contours extracted from computed flow fields.

wall and propagates intermittently, since the extent of LS-RZ decoupling is minor along the inner wall (see  $t = 108 - 116 \mu\text{s}$ ). These regions will be consumed by transverse waves propagating along the detonation front in the same fashion as for  $p_0 = 15 \text{ kPa}$ . Figure 8 also shows a closeup of this structure for  $p_0 = 26 \text{ kPa}$  case. Evidence of this intermittent behavior can be seen in the numerical soot foils and velocity histories shown in Figs. 4 and 6, respectively. Similarly to  $p_0 = 15 \text{ kPa}$ , the early stages of a Mach reflection along the inner wall appears at  $t = 123 \mu\text{s}$ , while on the outer wall, a stronger and smaller Mach stem forms that decreases rapidly and transitions into the regular reflection described in Fig. 3.

Finally, as the Mach stem along the inner wall continues to propagate into an ever-increasing area, full decoupling occurs irrespective of the initial pressure considered. However Fig. 10 shows that, for  $p_0 = 26 \text{ kPa}$ , this

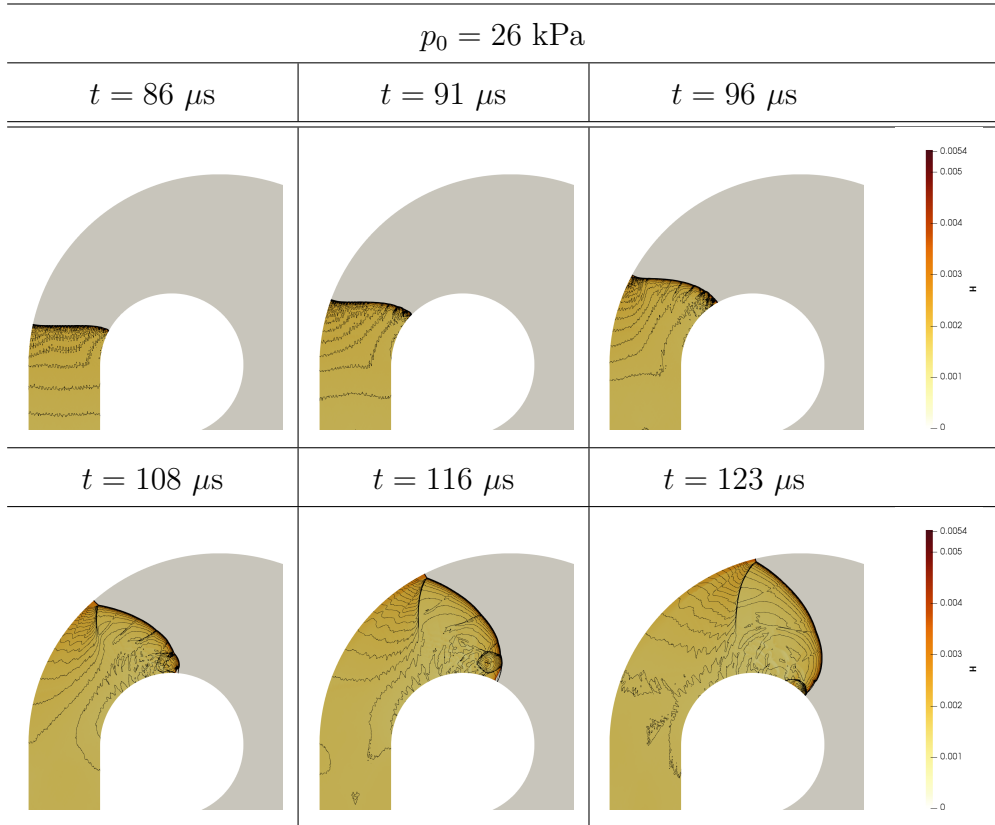


Figure 9: Early stages of detonation propagation for  $p_0 = 26 \text{ kPa}$ : numerical pressure contours and H atom field.

decoupling takes place earlier but further along the inner wall, which is simply a consequence of the increased initial density and associated differences in wave speeds.

#### 4.3. Late stages of propagation

Figure 11 shows a close-up of the late stages of detonation propagation in the curved chamber for  $p_0 = 15$  and  $26 \text{ kPa}$ .

The global dynamics for both pressures bear similarities with the pres-

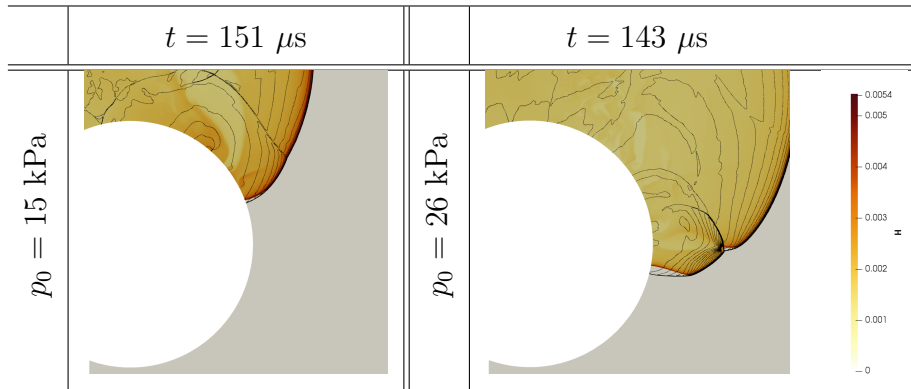


Figure 10: Location of full decoupling of leading shock and reaction zone along inner wall for increasing pressure.

ence of a regular reflection, a Mach detonation (stem), a decoupled LS-RZ, a transverse detonation wave, reflected waves, and shear layers. However, differences exist in the reflection transition location (regular-to-Mach) and final wave structure. The normalized critical angle,  $\theta_{\text{crit}}/\pi$ , where the decoupled LS-RZ interacts with the detonation wave propagating along the outer wall, depends on the decoupling of the diffracting detonation along the inner wall (Fig. 10). When full decoupling occurs, the LS velocity decreases significantly allowing for enough time for the detonation propagating along the outer wall to catch up, and for a Mach reflection to redevelop (see Fig. 11). A plot summarizing the normalized transition angles for all pressures considered is shown in Fig. 12;  $\theta_{\text{crit}}/\pi$  decreases with increasing pressure and seems to have an asymptote at about  $\theta_{\text{crit}}/\pi \sim -0.3$ .

The differences in wave structure at the very late stages of propagation,  $t = 236$  and  $196 \mu\text{s}$  for  $p_0 = 15$  and  $26 \text{ kPa}$ , respectively, seem to be simply a consequence of the location where transition occurs. In other words, the

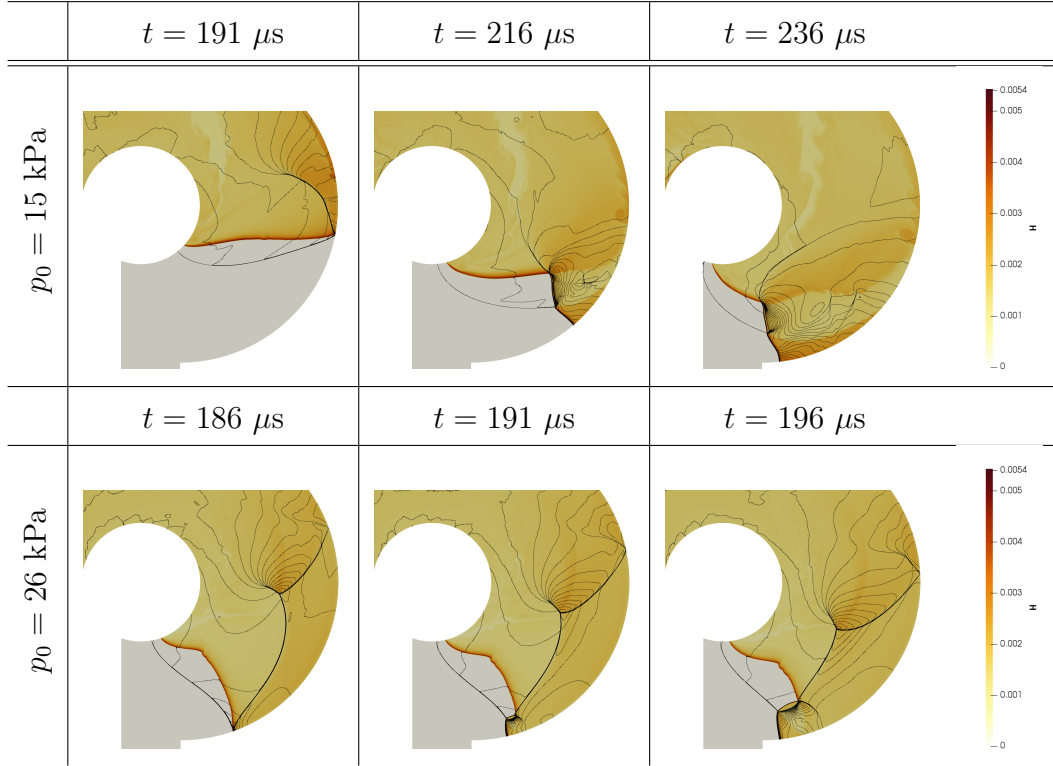


Figure 11: Late stages of detonation propagation for increasing pressure: numerical pressure contours and H atom field.

available arc length for propagation after transition,  $\Delta s = r_e(\theta_{\text{crit}}/\pi - \theta_{\text{end}}/\pi)$  – where  $r_e$  is the radius of the outer wall and  $\theta_{\text{end}}/\pi = -0.5$  is the angular location at which the outer wall meets the straight section of the chamber – is larger for  $p_0 = 15 \text{ kPa}$  (and  $p_0 = 10 \text{ kPa}$ ). This allows for the competition between the transverse detonation that propagates in shocked mixture and the rotating Mach stem propagating along the outer wall to last longer, and an “S-shape” arises as a result. Experimental evidence showing this wave structure is included in Fig. 13.

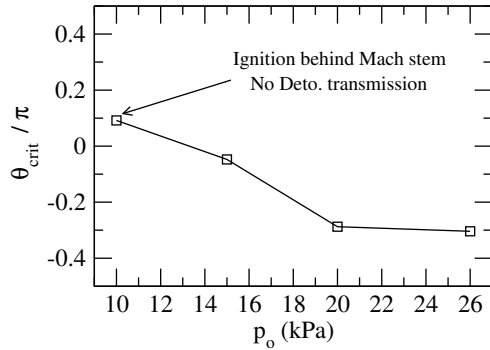


Figure 12: Critical normalized angle ( $\theta_{\text{crit}}/\pi$ ) as a function of pressure for transition from regular to Mach detonation along outer wall - numerical results.

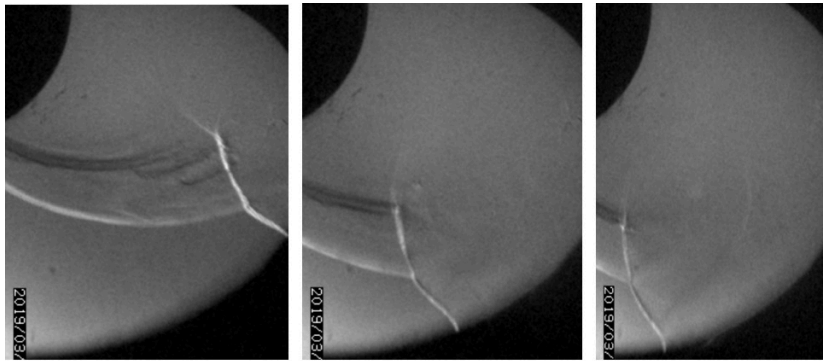


Figure 13: schlieren images showing “S-shape” wave structure during late stages of propagation in chamber -  $p_0 = 15$  kPa.

As mentioned in [9, 10], it is worth emphasizing that the evolution described above is a universal typical feature of re-initiation of diffracting detonations, and is not specific to the  $\text{H}_2\text{-O}_2\text{-Ar}$  mixture considered. Indeed, many experiments on detonation transmission from a straight channel to an open volume using different mixtures (see [40], for example), have identified a similar behavior (Fig. 14). The distinctiveness of the present work is

that the geometry plays an important role as the chamber is effectively an open, diverging volume bounded by a concave wall (which differs from classical diffraction experiments); as a result, the initially diffracting detonation turns into a rotating Mach detonation.

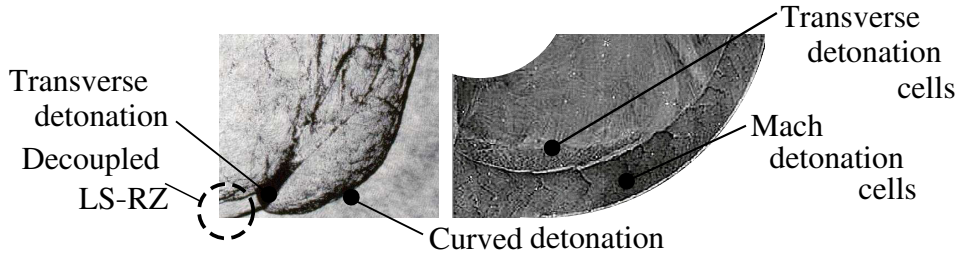


Figure 14: Experimental evidence of transverse detonation waves in different mixtures and geometries:  $0.5 \text{ H}_2 + 0.5 \text{ N}_2\text{O}$  for  $p_0 = 47.5 \text{ kPa}$  adapted from [40] (left) and  $\text{C}_3\text{H}_8 + 5 \text{ O}_2$  for  $p_0 = 12 \text{ kPa}$  adapted from [9, 10] (right).

#### 4.4. Re-initiation dynamics

A further decrease in pressure to  $p_0 = 10 \text{ kPa}$  resulted in the decoupling of the LS and RZ in the straight section of the chamber. This simply means that the amount of energy deposited in the gas through our numerical ignition scheme (described in subsection 3.2) was not sufficient to initiate a detonation directly. In contrast to the detonation transmission cases analyzed above, this case represents the re-initiation of a detonation by the transmission of an initially planar shock into the curved chamber. It should be noted that the numerical simulations first revealed the existence of this regime, and the accompanying experiments were run afterwards to validate the numerical predictions. To do so, the experimental setup was slightly modified. An additional  $18 - \mu\text{m}$  Mylar foil was used to separate the detonation tube from

the curved chamber (see Mylar 2 in Fig. 1). The interaction of the detonation with the Mylar foil resulted in a repeatable, normal transmitted shock into the straight section of the curved chamber (see schlieren image at  $t = 128 \mu\text{s}$  in Fig. 15).

Figure 15 shows the numerical and experimental re-initiation dynamics. The interaction of the normal shock with the curved section results in the development of an *inert* Mach stem along the outer wall, and a diffracted curved shock along the inner wall at  $t = 155 \mu\text{s}$ . The thermodynamic state, i.e., pressure and temperature ratios, behind the Mach stem are  $p/p_0 \sim 23$  and  $T/T_0 \sim 4.7$ , whose associated delay time is less than  $1 \mu\text{s}$ . Consequently, an ignition center forms close to the wall (see fields at  $t = 158 \mu\text{s}$ ). Although the inviscid formulation used in this work is only capable of capturing purely chemical ignitions, since thermal and hydrodynamic boundary layers are not part of the computed flow field, the agreement observed with the experimental sequences indicates that chemistry is dominant over diffusive effects in this regime.

The interaction of the curved shock, that develops from the explosion, with the previously shocked mixture and Mach stem initiates a detonation. The early stages of this transient are shown at  $t = 166 \mu\text{s}$ . The initially straight Mach stem has now become a curved detonation moving upstream, and the ignition center has similarly developed into an additional detonation propagating downstream. A larger transverse detonation, whose structure was already depicted in Fig. 8, consumes the mixture behind the curved diffracted shock (see  $t = 180 \mu\text{s}$ ) to become a slightly curved detonation that takes the full extent of the chamber at  $t = 196 \mu\text{s}$ .

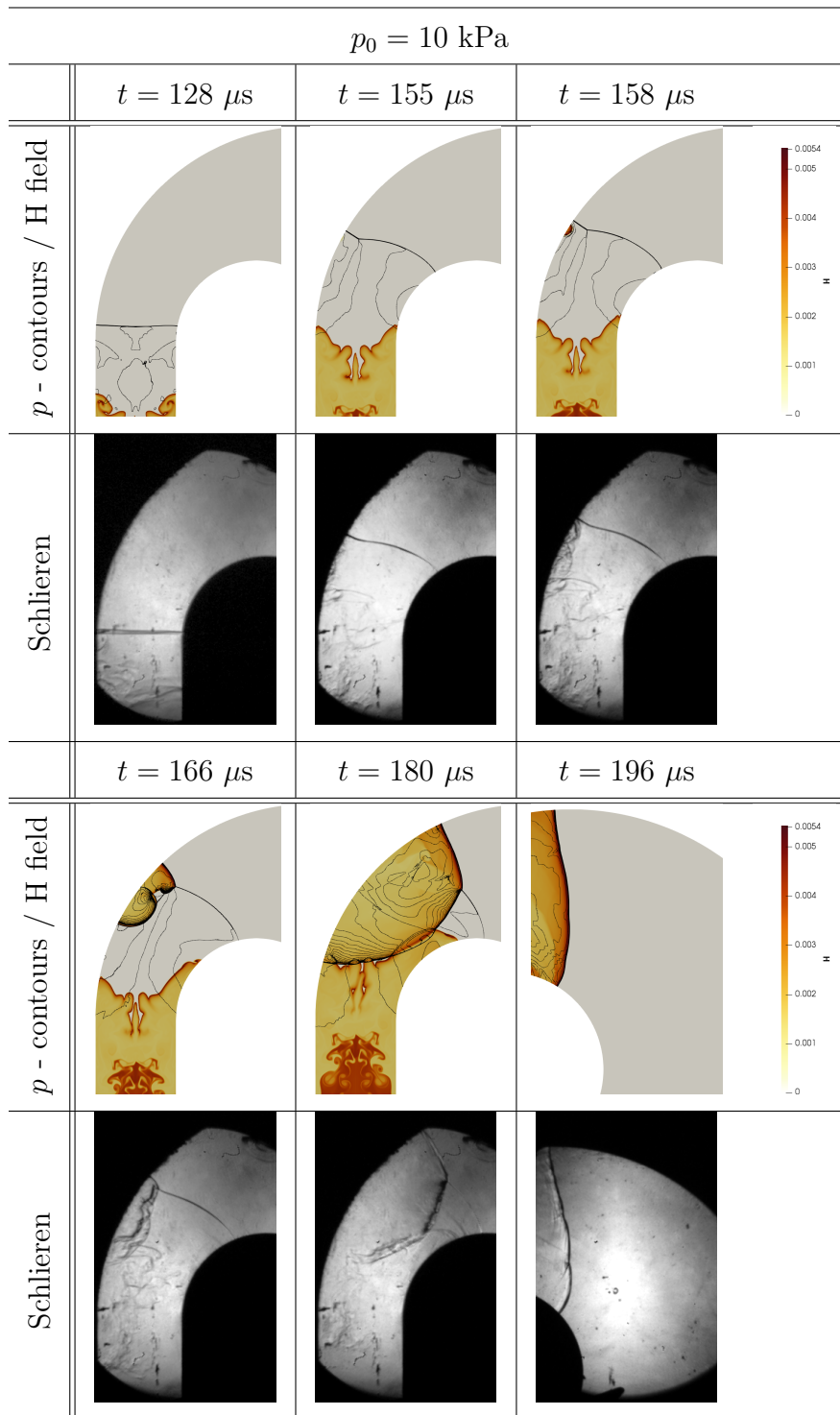


Figure 15: Re-initiation dynamics for  $p_0 = 270 \text{ kPa}$ : numerical pressure contours and H atom field vs. experimental hi-speed schlieren.

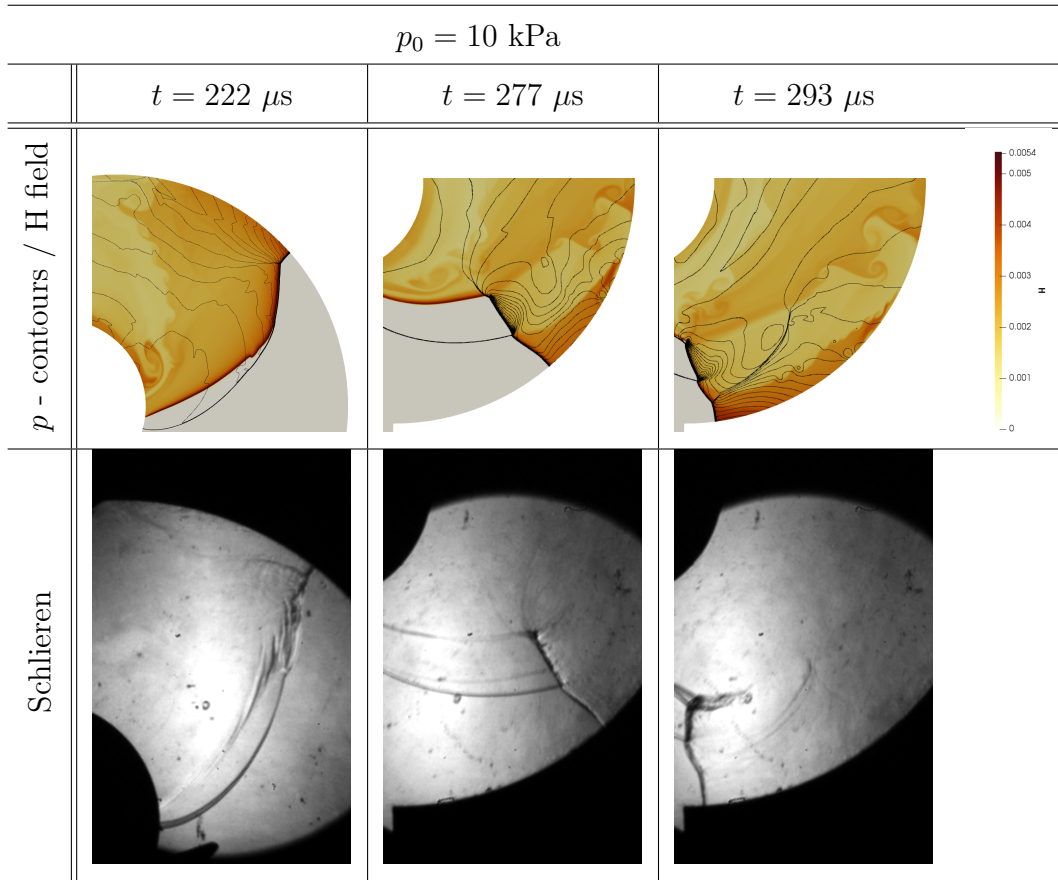


Figure 16: Late stages of detonation propagation for  $p_0 = 10 \text{ kPa}$ : numerical pressure contours and H atom field vs. experimental hi-speed schlieren.

The late stages of the process in the curved chamber are shown in Fig. 16; the intermediate dynamics are the same as described above for  $p_0 = 15$  kPa, except that the transition from regular to Mach detonation occurs earlier at  $\theta_{\text{crit}}/\pi \sim 0.1$  (see Fig. 10). The experimental observations are in remarkable agreement with the numerical predictions regarding the wave dynamics, curvatures, separation distances between reaction zones and decoupled leading diffracted shocks, transverse detonation wave angles, and final wave structures at all time instances shown. The success in capturing the experimentally observed dynamics as a function of pressure using an inviscid formulation, that does not deliberately resolve the detonation cellular structure in the highly compressed regions of the chamber, demonstrates that the main drivers dictating the global features in the chamber are the geometry and the initial pressure.

To substantiate this hypothesis we used the latter experimental methodology but filled the chamber with air, whose ratio of specific heats,  $\gamma$ , is close to that of the argon-diluted stoichiometric  $\text{H}_2\text{-O}_2$  mixture studied (5% lower). The results are shown in Fig. 17; the similarities with the reactive cases discussed throughout this manuscript are evident. A more comprehensive experimental and numerical study of the inert wave dynamics as a function of  $\gamma$  is currently being carried out and will be the object of a future submission.

## 5. Conclusion

Experiments and two-dimensional Euler simulations with detailed kinetics were performed to characterize, as a function of initial pressure, the deto-

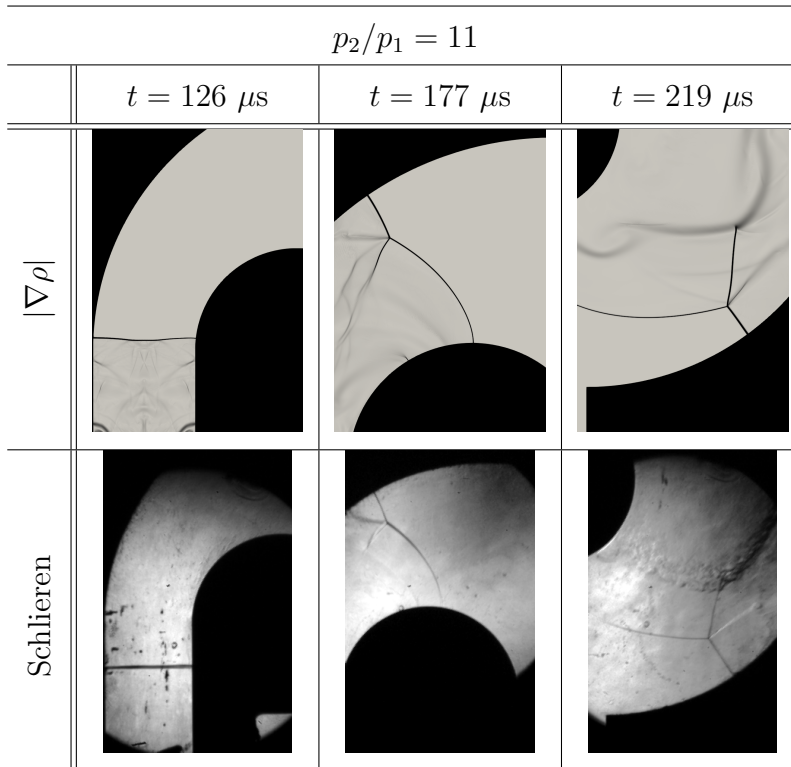


Figure 17: Inert case: transmission of a shock wave (measured wave speed:  $u_s = 1067$  m/s; computed pressure ratio:  $p_2/p_1 = 11$ ) into the curved chamber filled with air; magnitude of density gradient,  $|\nabla \rho|$  (numerical) vs. experimental schlieren.

nation transmission from a straight channel into a curved chamber using an argon-diluted (40%) stoichiometric H<sub>2</sub>-O<sub>2</sub> mixture. All computed behaviors show a very complex dynamics that superimposes almost exactly to those identified in the experiments. This demonstrates the validity of the assumptions of the chosen numerical methodology.

Early stages of the evolution included decoupling and re-initiation of the diffracting detonation along the inner wall of the chamber, formation of a Mach stem whose height decreased as it propagated along the outer wall, and transition to regular reflection. At later times, full decoupling of the diffracting detonation occurred along the inner wall, and, along the outer wall, an additional transition to a rather complex wave structure took place composed of a Mach detonation, a decoupled LS-RZ, a transverse detonation, reflected waves and shear layers. A pressure increase from 10 to 26 kPa resulted in differences in the reflection transition location,  $\theta_{\text{crit}}/\pi$ , velocities of the discontinuities and final wave structure. Notably,  $\theta_{\text{crit}}/\pi$  seems to asymptote with increasing pressure, likely due to having a curved chamber of finite length. These results confirm, as well as preliminary inert experiments and simulations, that while the transient phenomena occurring along the outer wall at early times seemed to be largely influenced by the dynamics of the LS-RZ complex propagating along the inner wall, once the final state was engaged, the global dynamics and the rotating Mach detonation in the chamber are mostly driven by geometry and initial pressure.

We chose a numerical resolution that does not resolve the cellular structure in the highly compressed regions behind the detonation Mach stem and transverse detonation. The agreement obtained with the experiments sup-

ports our previous conclusion [9, 10] that resolving all the details of the detonation structure are not essential to capture the intricate transients experimentally observed. Finally, our results also support the applicability of GSD modeling [20] or variations thereof [41, 42] for the analysis of the current configuration, if one is only interested in capturing the most salient features of the dynamics.

### **Acknowledgements**

Computations were carried out on the supercomputer facilities of the Mésocentre de Calcul de Poitou Charentes. Experiments were conducted in the Detonation Team of the Institut Pprime UPR 3346 CNRS. This work was supported by a CPER FEDER Project of Région Nouvelle Aquitaine. Special thanks to Alain Claverie CNRS Research Engineer for his invaluable technical assistance.

### **References**

- [1] F. K. Lu, E. M. Braun, Rotating detonation wave propulsion: experimental challenges, modeling, and engine concepts, *Journal of Propulsion and Power* 30 (2014) 1125–1142.
- [2] P. Wolański, Detonative propulsion, *Proceedings of the combustion Institute* 34 (2013) 125–158.
- [3] K. Kailasanath, Review of propulsion applications of detonation waves, *AIAA Journal* 38 (2000) 1698–1708.

- [4] G. Ciccarelli, S. Dorofeev, Flame acceleration and transition to detonation in ducts, *Progress in energy and combustion science* 34 (2008) 499–550.
- [5] S. Hansmetzger, R. Zitoun, P. Vidal, A study of continuous rotation modes of detonation in an annular chamber with constant or increasing section, *Shock Waves* 28 (2018) 1065–1078.
- [6] J. Sousa, J. Braun, G. Paniagua, Development of a fast evaluation tool for rotating detonation combustors, *Applied Mathematical Modelling* 52 (2017) 42–52.
- [7] D. A. Schwer, R. F. Johnson, A. Kercher, D. Kessler, A. T. Corrigan, Progress in efficient, high-fidelity, rotating detonation engine simulations, in: *AIAA Scitech 2019 Forum*, p. 2018.
- [8] Z. Pan, B. Fan, X. Zhang, M. Gui, G. Dong, Wavelet pattern and self-sustained mechanism of gaseous detonation rotating in a coaxial cylinder, *Combustion and Flame* 158 (2011) 2220–2228.
- [9] V. Rodriguez, C. Jourdain, P. Vidal, R. Zitoun, An experimental evidence of steadily-rotating overdriven detonation, *Combustion and Flame* 202 (2019) 132–142.
- [10] V. Rodriguez, P. Vidal, R. Zitoun, Experimental observations of semi-confined steadily-rotating detonation, in: *Proc. of the 26th Int. Colloquium on the Dynamics of Explosions and Reactive Systems*. Boston, USA (1084).

- [11] V. Katta, K. Cho, J. Hoke, J. Codoni, F. Schauer, W. Roquemore, Effect of increasing channel width on the structure of rotating detonation wave, *Proceedings of the Combustion Institute* 37 (2019) 3575–3583.
- [12] Y. Sugiyama, Y. Nakayama, A. Matsuo, H. Nakayama, J. Kasahara, Numerical investigations on detonation propagation in a two-dimensional curved channel, *Combustion Science and Technology* 186 (2014) 1662–1679.
- [13] H. Nakayama, J. Kasahara, A. Matsuo, I. Funaki, Front shock behavior of stable curved detonation waves in rectangular-cross-section curved channel, *Proceedings of the Combustion Institute* 34 (2013) 1936–1947.
- [14] M. Short, J. J. Quirk, C. D. Meyer, C. Chiquete, Steady detonation propagation in a circular arc: a detonation shock dynamics model, *Journal of Fluid Mechanics* 807 (2016) 87–134.
- [15] M. Short, J. J. Quirk, C. Chiquete, C. D. Meyer, Detonation propagation in a circular arc: reactive burn modelling, *Journal of Fluid Mechanics* 835 (2018) 970.
- [16] M. Short, C. Chiquete, J. J. Quirk, Propagation of a stable gaseous detonation in a circular arc configuration, *Proceedings of the Combustion Institute* 37 (2019) 3593–3600.
- [17] G. Edward, R. Williams, Detonation interaction with wedges and bends, *Combustion Science and Technology* 11 (2002) 481–492.

- [18] S. Frolov, V. Aksenov, I. Shamshin, Shock wave and detonation propagation through u-bend tubes, *Proceedings of the Combustion Institute* 31 (2007) 2421–2428.
- [19] N. R. Council, et al., *Lessons learned from the Fukushima nuclear accident for improving safety of US nuclear plants*, National Academies Press, 2014.
- [20] C. Jourdain, V. Rodriguez, P. Vidal, R. Zitoun, Progress in understanding rotating detonation modes, in: *AIAA Scitech 2019 Forum*, San Diego, CA, p. 0200.
- [21] M. Zhao, D. Buttsworth, R. Choudhury, Experimental and numerical study of OH\* chemiluminescence in hydrogen diffusion flames, *Combustion and Flame* 197 (2018) 369 – 377.
- [22] Y. Hidaka, S. Takahashi, H. Kawano, M. Suga, W. C. Gardiner, Shock-tube measurement of the rate constant for excited hydroxyl (A2.SIGMA.+) formation in the hydrogen-oxygen reaction, *The Journal of Physical Chemistry* 86 (1982) 1429–1433.
- [23] T. Kathrotia, M. Fikri, M. Bozkurt, M. Hartmann, U. Riedel, C. Schulz, Study of the H+O+M reaction forming oh: Kinetics of OH chemiluminescence in hydrogen combustion systems, *Combustion and Flame* 157 (2010) 1261 – 1273.
- [24] D. Gutman, R. W. Lutz, N. F. Jacobs, E. A. Hardwidge, G. L. Schott, Shock-tube study of oh chemiluminescence in the hydrogen–oxygen reaction, *The Journal of Chemical Physics* 48 (1968) 5689–5694.

- [25] A. Burcat, B. Ruscic, et al., Third millenium ideal gas and condensed phase thermochemical database for combustion (with update from active thermochemical tables)., Technical Report, Argonne National Lab.(ANL), Argonne, IL (United States), 2005.
- [26] H. Weller, G. Tabor, H. Jasak, C. Fureby, A tensorial approach to computational continuum mechanics using object-oriented techniques, *Comput. Phys.* 12 (1998) 620–631.
- [27] R. Mével, S. Javoy, F. Lafosse, N. Chaumeix, G. Dupré, C. Paillard, Hydrogen-nitrous oxide delay time: shock tube experimental study and kinetic modelling, *Proc. Combust. Inst.* 32 (2009) 359–366.
- [28] A. Kurganov, E. Tadmor, New high-resolution central schemes for non-linear conservation laws and convection–diffusion equations, *Journal of Computational Physics* 160 (2000) 241–282.
- [29] A. Kurganov, S. Noelle, G. Petrova, Semidiscrete central-upwind schemes for hyperbolic conservation laws and Hamilton–Jacobi equations, *SIAM Journal on Scientific Computing* 23 (2001) 707–740.
- [30] M. Kraposhin, A. Bovtrikova, S. Strijhak, Adaptation of Kurganov-Tadmor numerical scheme for applying in combination with the PISO method in numerical simulation of flows in a wide range of Mach numbers, *Procedia Computer Science* 66 (2015) 43–52.
- [31] C. Romick, T. Aslam, J. Powers, The effect of diffusion on the dynamics of unsteady detonations, *Journal of fluid mechanics* 699 (2012) 453.

- [32] M. Kaneshige, J. E. Shepherd, Detonation database: GALCIT Report FM97-8, California Institute of Technology (1997).
- [33] B. Taylor, D. Kessler, V. Gamezo, E. Oran, The influence of chemical kinetics on the structure of hydrogen-air detonations, in: 50th AIAA Aerospace Sciences Meeting including the New Horizons Forum and Aerospace Exposition, p. 979.
- [34] L. Shi, H. Shen, P. Zhang, D. Zhang, C. Wen, Assessment of vibrational non-equilibrium effect on detonation cell size, *Combustion Science and Technology* 189 (2017) 841–853.
- [35] R. Mével, D. Davidenko, F. Lafosse, N. Chaumeix, G. Dupré, C.-É. Paillard, J. E. Shepherd, Detonation in hydrogen–nitrous oxide–diluent mixtures: An experimental and numerical study, *Combustion and Flame* 162 (2015) 1638–1649.
- [36] H. Hornung, Regular and Mach reflection of shock waves, *Annual Review of Fluid Mechanics* 18 (1986) 33–58.
- [37] X. Yuan, J. Zhou, X. Mi, H. Ng, Numerical study of cellular detonation wave reflection over a cylindrical concave wedge, *Combustion and Flame* 202 (2019) 179–194.
- [38] M. Reynaud, F. Virot, A. Chinnayya, A computational study of the interaction of gaseous detonations with a compressible layer, *Physics of Fluids* 29 (2017) 056101.

- [39] S. Taileb, J. Melguizo-Gavilanes, A. Chinnayya, Influence of the chemical modeling on the quenching limits of gaseous detonation waves confined by an inert layer, *Combustion and Flame* 218 (2020) 247–259.
- [40] F. P. Pintgen, Detonation diffraction in mixtures with various degrees of instability, Ph.D. thesis, California Institute of Technology, 2005.
- [41] X. Yuan, X. Mi, H. Ng, J. Zhou, A model for the trajectory of the transverse detonation resulting from re-initiation of a diffracted detonation, *Shock Waves* 30 (2020) 13–27.
- [42] X. Yuan, J. Zhou, S. Liu, Z. Lin, Diffraction of cellular detonation wave over a cylindrical convex wall, *Acta Astronautica* 169 (2020) 94–107.